energies

MDPI

Article

Experimental and Numerical Investigations of the Effect of Charge Motion on Abnormal Combustion in a Heavy-Duty H_2 DI ICE

Pascal Zimmer *, Moritz Lückerath and Stefan Pischinger

Chair of Thermodynamics of Mobile Energy Conversion Systems (TME), RWTH Aachen University, 52074 Aachen, Germany; lueckerath@tme.rwth-aachen.de (M.L.)
* Correspondence: zimmer@tme.rwth-aachen.de; Tel.: +49-2418048282

Abstract

In modern hydrogen engines, abnormal combustion phenomena such as knock and pre-ignition limit the operational range. To overcome these limitations, the balance of required and supplied ignition energy needs to be understood. Charge motion is one way to increase the robustness against abnormal combustion in conventional spark-ignition engines. Hence, test bench measurements with three different cylinder heads on a 2.13 L research single-cylinder engine are presented and analyzed, focusing on high loads up to IMEP = 32 bars. These cylinder heads are derived from a commercial heavy-duty diesel engine and feature different intake port designs, ranging from a filling to a tumble port design. 3D-CFD simulations enable deeper insight into charge motion, homogenization, turbulence intensity and temperature distribution and are used to understand the influence of different port and spray-forming cap designs on mixture formation and combustion characteristics. The results show that, depending on injection configuration, increased charge motion can decrease or increase NO_x emissions significantly but increases abnormal combustion tendency in all configurations by heating up the cylinder charge. This shows that significantly increased charge motion is not necessarily required for retrofitted heavy-duty hydrogen engines to reach diesel-like performance.

Keywords: hydrogen; combustion; charge motion; CFD; simulation; spark ignition; direct injection; knock; pre-ignition; abnormal combustion

Academic Editor: Maria Founti

Received: 30 September 2026
Revised: 19 October 2026
Accepted: 30 October 2026
Published: 3 November 2026

Copyright: © 2026 by the authors. Licensee MDPI, Basel, Switzerland. This article is an open access article distributed under the terms and conditions of the Creative Commons Attribution (CC BY) license.

1. Introduction

The power density in spark-ignited (SI) heavy-duty (HD) hydrogen (H_2) engines is usually limited by the occurrence of abnormal combustion. To achieve engine performance competitive with conventional diesel engines, it is important to understand the mechanisms behind abnormal combustion [1–4]. For direct-injection combustion systems, knock and pre-ignition (PI) are the relevant phenomena and occur depending on boundary conditions. Knock describes the autoignition of the mixture after (spark) ignition in the end-gas region, whereas PI describes the autoignition of the mixture before spark ignition. Knock and PI can occur simultaneously, often resulting in very high knock amplitudes, posing a significant limitation for safe engine operation in regular series production engines [5,6]. Regardless of the type of abnormal combustion, the ignition energy supplied to the mixture must always be greater than the ignition energy required by the

mixture at given boundary conditions. The required ignition energy depends on the temperature, pressure, gas composition (EGR, lambda, and humidity) and geometry of the ignition source [7–10].

Recent studies on HD H_2 engines have focused mainly on ignition, injection, and boosting systems [11–14], valve timing, or exhaust gas recirculation (EGR) [15] and their influence on abnormal combustion. Only a few publications have discussed the influence of charge motion on the combustion process and the occurrence of knock and pre-ignition. Furthermore, only a limited number of studies have incorporated testing of different turbulence levels on an HD engine [16], as most publications on this topic are based on simulations [17,18]. Most of these publications investigated only mid- to low-load operation. High-load investigations comparable to the operational range presented in this paper are rare [19]. The current state of research highlights the novelty of the presented results, as they combine the experimental investigations of different intake port designs with high-load operation that can compete with modern diesel engines regarding power density.

The gas composition is one of the most important factors discussed in this work. As the local lambda has a significant influence on the required ignition energy, mixture formation represents one of the most relevant areas for optimization. In Figure 1, the correlation between minimum ignition energy (MIE) and lambda is shown. Comparing $\lambda = 1$ as a baseline to $\lambda = 2.5$ and $\lambda = 4$, the MIE increases to ~140% and ~465%, respectively, illustrating the effect of local lambda on the ignitability of the mixture. The comparison with methane illustrates the high ignitability of hydrogen and displays its wide flammability limits.

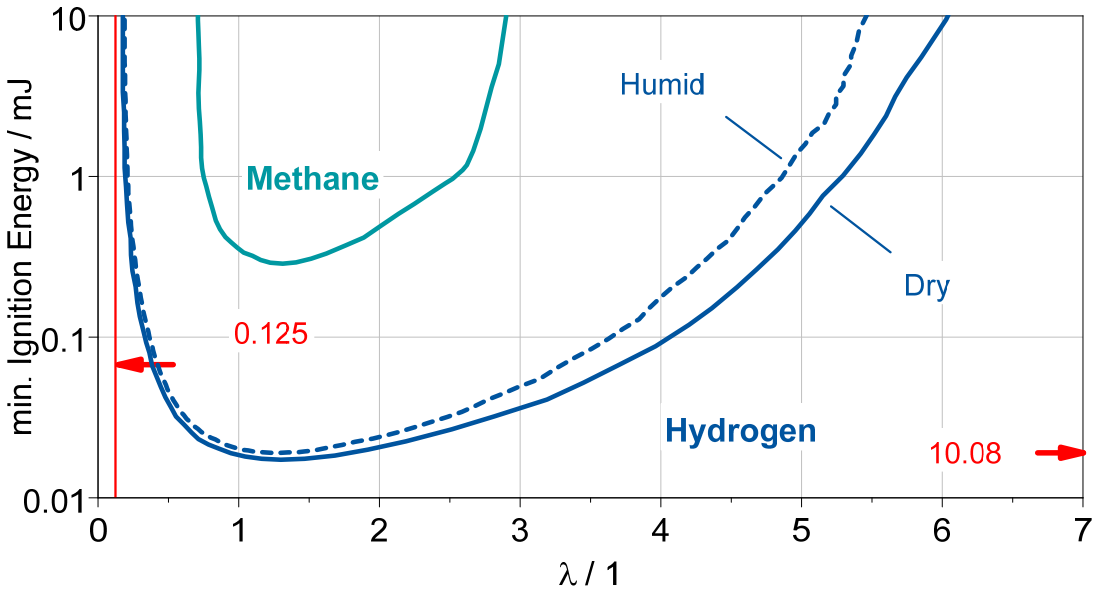


Figure 1. Minimum ignition energy of hydrogen and methane as a function of lambda [20,21].

In this paper, the influence of charge motion on abnormal combustion, emission formation, and combustion characteristics is discussed using test bench measurement data acquired on a 2.13 L single-cylinder research engine (SCE). Three cylinder heads with different levels of charge motion (Tumble), realized by intake port design modifications, are compared. The results show that the interaction between injection configuration and intake port design influences the quality of the combustion significantly. These measurements are accompanied by 3D-CFD simulations focusing on intake flow, injection, and mixture formation. The 3D-CFD simulations, thereby, visualize the interaction between

the charge motion and the injection for the different geometries and allow for a deeper interpretation and understanding of the experimental results.

This study shows that a general increase in charge motion is not the only solution approach to reach higher power. As mixture formation is the main goal to improve robustness, charge motion is not required if a high level of homogenization can be achieved by injection and combustion chamber design. In this case, higher charge motion can be harmful regarding abnormal combustion by heating the mixture more than with lower charge motion. Previous studies on this engine and published research suggest that increasing charge motion by a small margin (base port to tumble blends) is beneficial, which is supported by the results of this paper. The high-load range of this engine, combined with its size and high levels of turbulence (tumble port), has not been investigated in other publications so far. The positive effects of high charge motion outweigh the negative ones in low- to medium-power applications and may play a different role in smaller engines [2,22].

2. Materials and Methods

2.1. Experimental Setup

The measurements were conducted on a 2.13 L direct-injection single-cylinder research engine. This engine was derived from a commercial diesel engine with a flat flame deck. A piston with a pot bowl and a compression ratio (CR) of 10.6:1, as well as new cylinder heads with a lateral injector port, were designed to create an SI combustion system that can operate on H_2. The engine specifications are listed in Table 1.

Table 1. Engine specifications.

Specification	Unit	Description/Value
Bore x stroke	mm	132 × 156
Displacement	dm^3	2.13
Compression ratio	-	10.6:1
Peak firing pressure	bar	Cylinder head: 300 bar; piston: 250 bar
Rail pressure H_2	bar	0–50
Injector	-	Bosch HIDI CV high flow
Piston	-	Pot bowl prototype with specialized piston ring package
Injection system	-	Low-pressure direct injection
Ignition	-	Cold M14x26.5 mm ring electrode spark plug (Burscheid GmbH, Burscheid, Germany)
Engine control unit	-	dSPACE
Cylinder pressure sensor	-	Kistler 6041B (Kistler Instumente AG, Winterthur, Switzerland)
Charge amplifier	-	Kistler 5064C (Kistler Instumente AG, Winterthur, Switzerland)
Exhaust pressure sensor	-	Kistler 4049B10 (Kistler Instumente AG, Winterthur, Switzerland)
Intake pressure sensor	-	Kistler 4045A10 (Kistler Instumente AG, Winterthur, Switzerland)
Piezoresistive amplifier	-	Kistler 4665 (Kistler Instumente AG, Winterthur, Switzerland)
Signal conditioning unit	-	Kistler SCP 2853 (Kistler Instumente AG, Winterthur, Switzerland)
Incremental encoder	-	Leine Linde Type 503 (Leine Linde AB, Strängnäs, Sweden)
Resolution of encoder	-	3600 pulses/rev = 0.1° CA increments

Indication system	-	FEVIS

The engine features a lateral injector position for direct injection with two different spray-forming caps (SFCs) that are mounted in the cylinder head. This design is advantageous for research applications, as variations in spray targeting are possible without commissioning a new injector with an integrated nozzle. The layout of the engine is displayed in Figure 2. The cylinder pressure sensor is mounted flush with the flame deck to avoid acoustic fluctuations. The cold M14 spark plug with a ring electrode without any precious metal is mounted in the center of the combustion chamber.

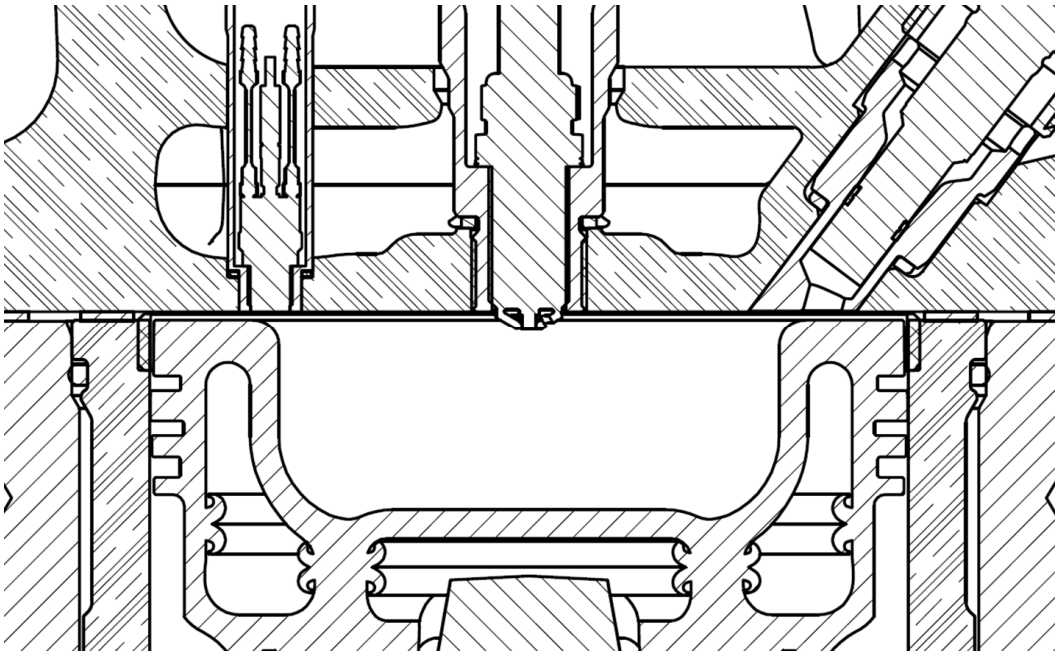


Figure 2. Combustion chamber layout.

Figure 3 shows the two SFC designs that were tested and simulated. The spray targeting of the angled SFC aims at the center of the piston bowl to avoid the creation of oil droplets due to the interaction of the H_2 jet with the oil in the top land. The axial SFC is a design with strong jet penetration and higher momentum preservation compared with the redirected spray of the angled SFC.

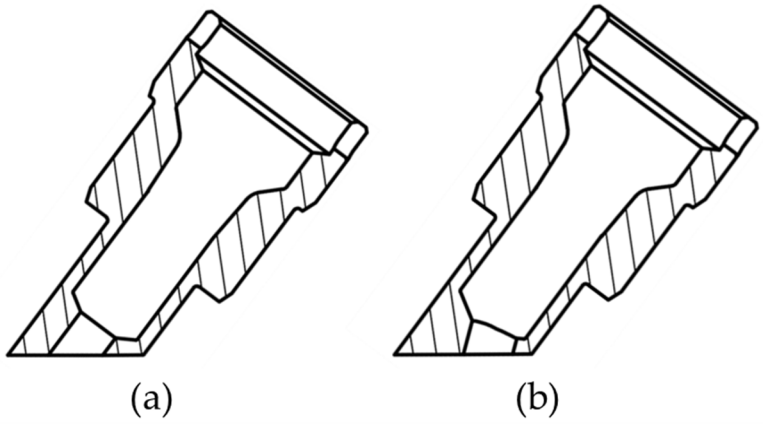


Figure 3. (**a**) Axial and (**b**) angled spray-forming caps.

The original intake port resembles a conventional filling port without any charge motion. Derived from the diesel engine, this port serves as the baseline and will be referred

to as the base port (BP). This port was then equipped with tumble blends (TBs). These are plates that are mounted before the seat rings are fitted into the cylinder head and are designed to create moderate tumble charge motion. The third head features specifically designed tumble ports (TPs) to create a higher tumble level than the tumble blends. The cutaways of the ports are displayed in Figure 4.

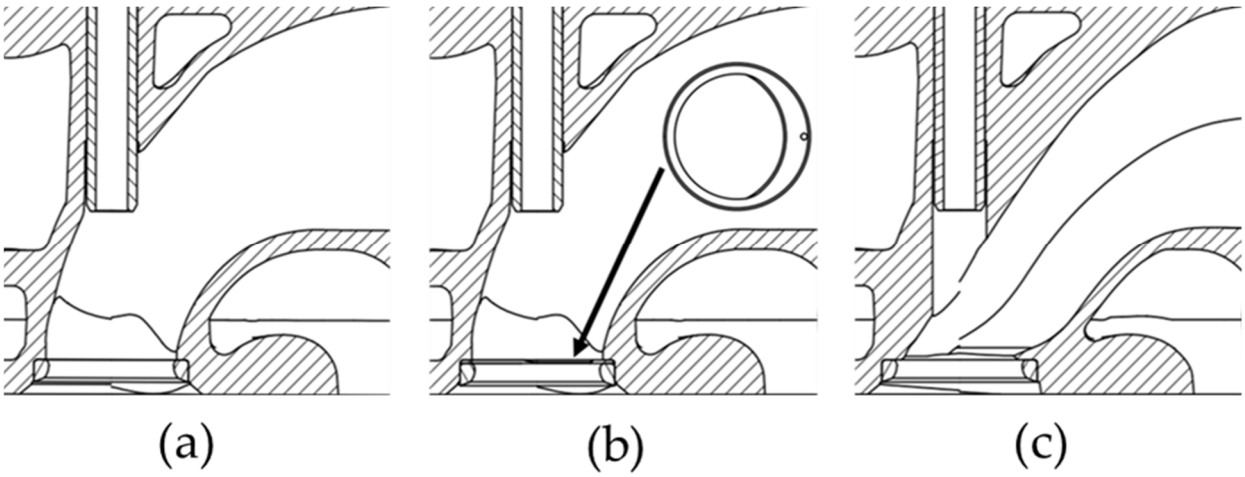


Figure 4. Investigated intake port designs: (**a**) base port; (**b**) base port with tumble blend; and (**c**) tumble port.

To further illustrate the relative alignment of the individual components, Figure 5 shows a 3D visualization of the combustion chamber. On the right side, the intake port is shown in light blue, the injector is visible on the left in orange, and the spark plug is illustrated centrally in gray. The dark blue areas depict the cooling channels. The coordinate system at the bottom aligns with the orientation of the 3D-CFD simulation model.

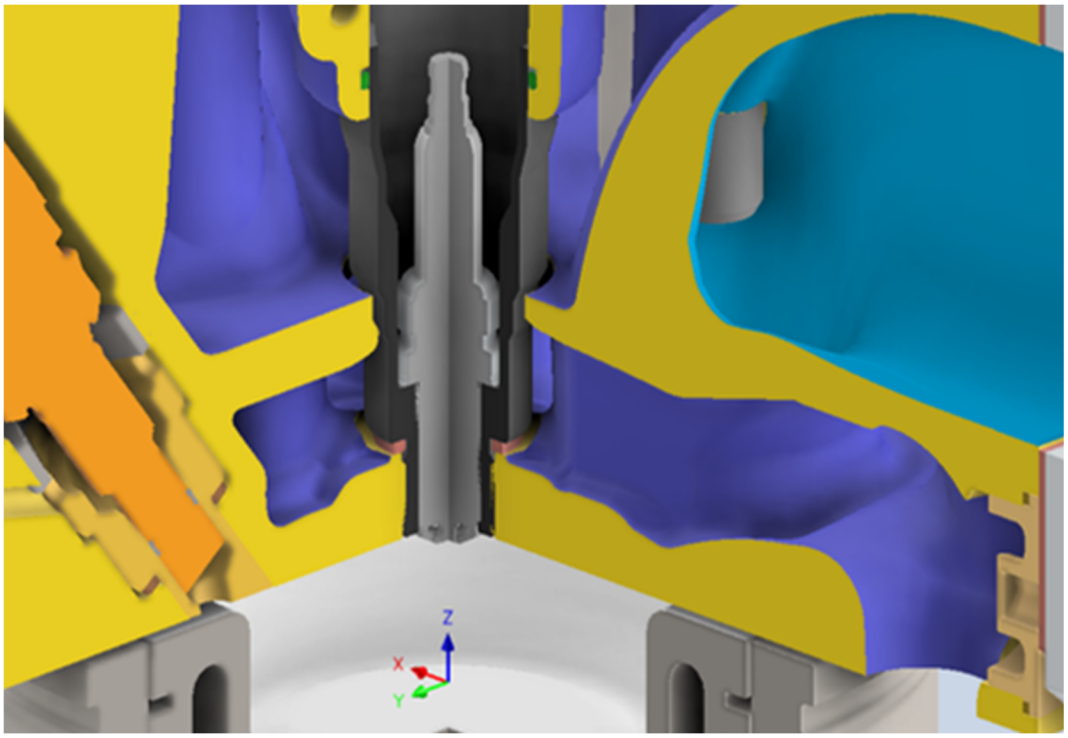


Figure 5. 3D visualization of the combustion chamber layout with the corresponding coordinate system.

Figure 6 displays simulations of the stationary tumble number of the three designs. The typical trade-off between filling and charge motion becomes clearly visible. The flow coefficient is calculated as follows: $\alpha_K = \frac{\dot{m}_{real}}{\rho_s * c_s * A_,}$. Here, $\dot{m}_{real}$ is the actual mass flow through the valve, while the quotient calculates the ideal isentropic mass flow (density ρ_s and velocity s_s) through the piston area A_k. While the filling port reaches a flow coefficient close to 13%, the flow coefficient for the tumble port stagnates below 8%. The tumble port reaches a stationary tumble number of $TR_y = 2.5$, the tumble blend port achieves a value of around $T_y = 1.2$, whereas the filling port only attains $T_y = 0.9$. Figure 7 presents the tumble number around the y-axis from a 3D-CFD simulation for an engine speed of n = 1600 1/min and an indicated mean effective pressure of IMEP = 24 bar. The comparison between Figures 6 and 7 shows two different tumble values. In Figure 6, stationary values (simulated at a constant valve lift) are shown, whereas in Figure 7, tumble is calculated with a dynamic valve lift and a moving piston. While the stationary tumble number for the tumble blend port is only slightly higher than for the base port, it produces a clearly higher first tumble peak in the transient simulation. Only the dedicated tumble port produces a clear second tumble peak as well.

Although the intake port design influences the y-tumble motion heavily, the spray-forming cap has a negligible effect. This is due to the fact that the injector is not injecting into the y-tumble plane, but orthogonally to it, as Figure 2 shows. During the intake stroke, the port equipped with the tumble blends introduces more charge motion than the base port. However, the tumble motion dissipates quickly and is not preserved during the compression phase. This highlights that the tumble blends, being a non-optimized, retrofitted plate design, do not produce a clean tumble motion around the cylinder center. In comparison, the designated tumble port produces a much stronger tumble motion during the intake stroke that is preserved during compression.

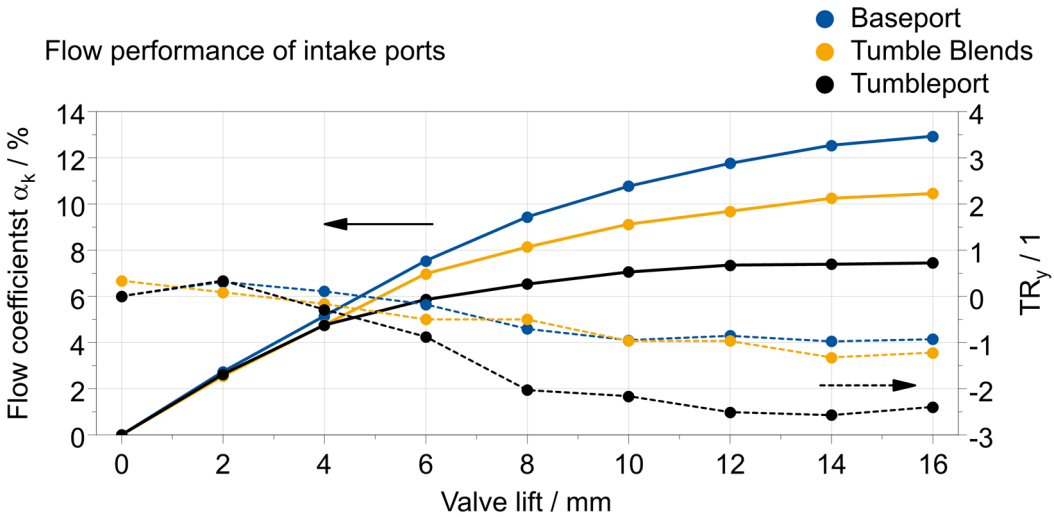


Figure 6. Flow performance and stationary tumble number of the intake ports from stationary CFD simulations for different valve lifts.

Figure 7 presents this tumble motion at the injection timing. The tumble rotates cleanly around the center. This was only achievable with the designated port design and not with the tumble plates. A clear second tumble peak is visible, and the motion only dissipates into turbulence in the late compression phase. At top dead center (TDC) (720 degrees crank angle (°CA)), the tumble flow is still much stronger when compared with the BP and TB designs.

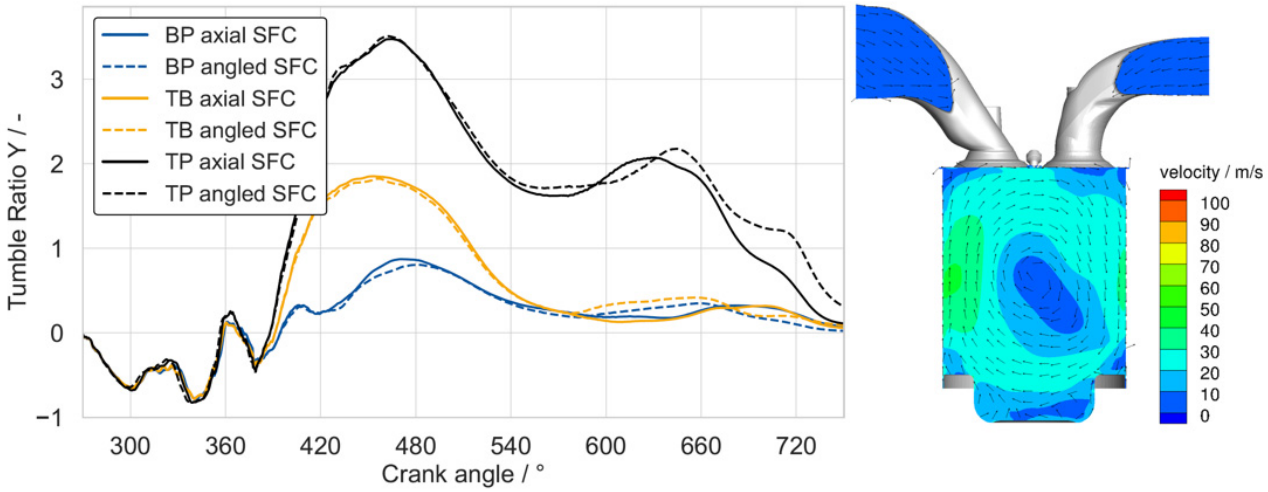


Figure 7. Transient tumble number development for all configurations of intake ports (BP, TB and TP with axial and angled SFC each) and visualization for the tumble port flow field at injection timing SOI = 150 °CAbTDC.

2.2. CFD Setup

All 3D-CFD simulations are transient RANS simulations conducted using the commercial software Converge CFD v3.0.28 [23]. The simulations focus on the gas exchange, the injection and the mixing process. The resulting quantities, especially mixture homogeneity, are then employed to further explain the experimental results. Table 2 summarizes the key settings of the numerical model. For the injection and mixing of hydrogen, it is especially important to account for the different diffusivities of each species. Therefore, the "mixture-averaged diffusivity" model is employed, which does not calculate a single diffusion coefficient for the entire fluid, but calculates individual diffusivities for each species in the domain [24,25].

Table 2. Settings of the 3D-CFD model.

Model Description	Specification
Turbulence model	k-epsilon RNG
Diffusion modeling	Mixture-averaged for each species
Convective CFL limit	1
Solver	Implicit density-based PISO, except for turbulence equations, all 2nd order
Wall modeling	O'Rourke and Amsden (standard wall function)
Temperature boundary condition	Law of the wall ($T_{Cylinderhead}$ = 546 K; T_{Liner} = 473 K; and T_{Piston} = 526 K)
Base grid size	4 mm
Smallest refinements	$4\ \text{mm}/2^3 = 0.5\ \text{mm}$
Hydrogen boundary conditions	Static mass flow of the injector $\dot{m}_{H2} = 17\frac{g}{s}$ Mass flow and valve lift are ramped up and down for $t_{ramp} = 0.5$ ms Injection duration at $n = 1600$ 1/min and $IMEP = 24$ bar: $Inj_{dur.}$ = 55 °CA

Adaptive mesh refinement is employed to keep the overall simulation efficient, while maintaining a high resolution in regions of high gradients. The total cell number reaches around 3 million. A mesh independence study was conducted in which the base mesh size was varied between $\Delta x = 3.5$ mm and $\Delta x = 8.0$ mm. The main challenge lies in resolving

the turbulent hydrogen injection jet. Previous studies have shown that an insufficiently fine resolution can lead to significant differences in the predicted jet penetration depth and shape [26–29]. To characterize the jet penetration and shape for all grid sizes studied, Figure 8 presents the jet penetration depth in both the z- and y-directions. The coarsest mesh ($\Delta x = 8$ mm) underestimates the overall jet penetration, whereas the medium base mesh sizes ($\Delta x = 5$ and 6 mm) lead to deviations in the jet shape in the y-direction. The three finest base mesh sizes ($\Delta x = 3.5, 4$ and 4.5 mm) do not differ significantly, indicating mesh convergence. However, as the mesh $\Delta x = 4.5$ mm (orange) still slightly overestimates the jet penetration depth in its later phase, the $\Delta x = 4$ mm base grid size (red) was used for all studies in this paper.

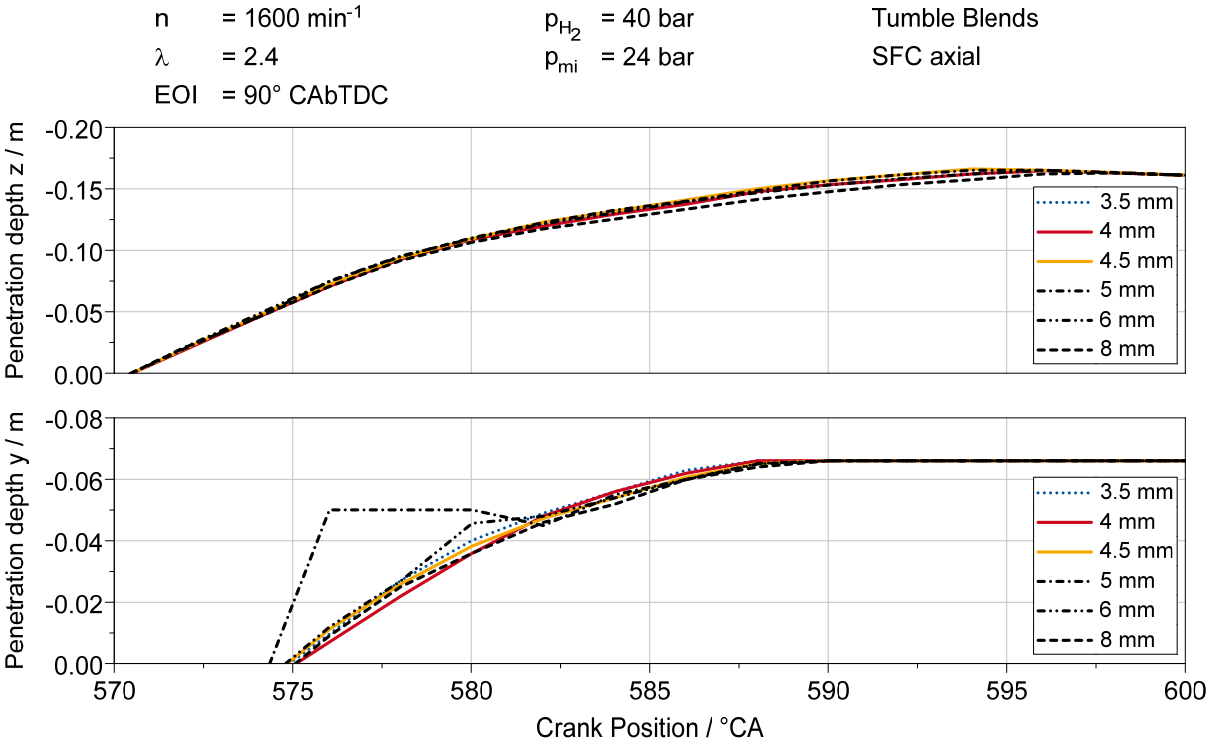


Figure 8. Results of the mesh independence study. The upper plot shows the hydrogen jet penetration in the z-direction; the lower plot shows the penetration in the y-direction. The result of the finest base mesh size ($\Delta x = 3.5$ mm) is shown by the dotted blue line. The base grid sizes of $\Delta x = 5, 6$ and 8 mm show significant deviations. A base grid size of $\Delta x = 4$ mm was used for all further numerical investigations. This study was conducted for the tumble blend port with the axial spray-guiding cap at an indicated mean effective pressure of IMEP = 24 bar.

Figure 9 shows an example of the discretization used. Large parts of the domain are discretized with the base grid size, while regions near walls and regions with high velocity or hydrogen concentration gradients are refined considerably.

Although a RANS turbulence model inherently produces averaged results and cannot resolve cycle-to-cycle variations, the in-cylinder turbulent kinetic energy (TKE) still allows different intake port designs to be compared: a higher TKE predicted by the RANS model indicates a higher intensity of turbulent fluctuations in the non-averaged real-world engine flow. An increase in TKE can, therefore, enhance mixing. This effect is captured by the mixture-averaged diffusivity model. The molecular diffusivity is enhanced by the turbulent diffusivity from the RANS model [23].

The mixture homogeneity predicted by the RANS simulation represents only an average cycle and is not representative of individual engine cycles. However, multiple studies have shown that a poorer average mixture homogeneity (e.g., from RANS simulations

or from averaged optical experiments) correlates well with worse engine performance in terms of combustion stability and NO_x emissions [30–32]. The CFD results in this paper can, therefore, be used to compare the mixture formation across the different engine concepts and to help explain the test-bench results.

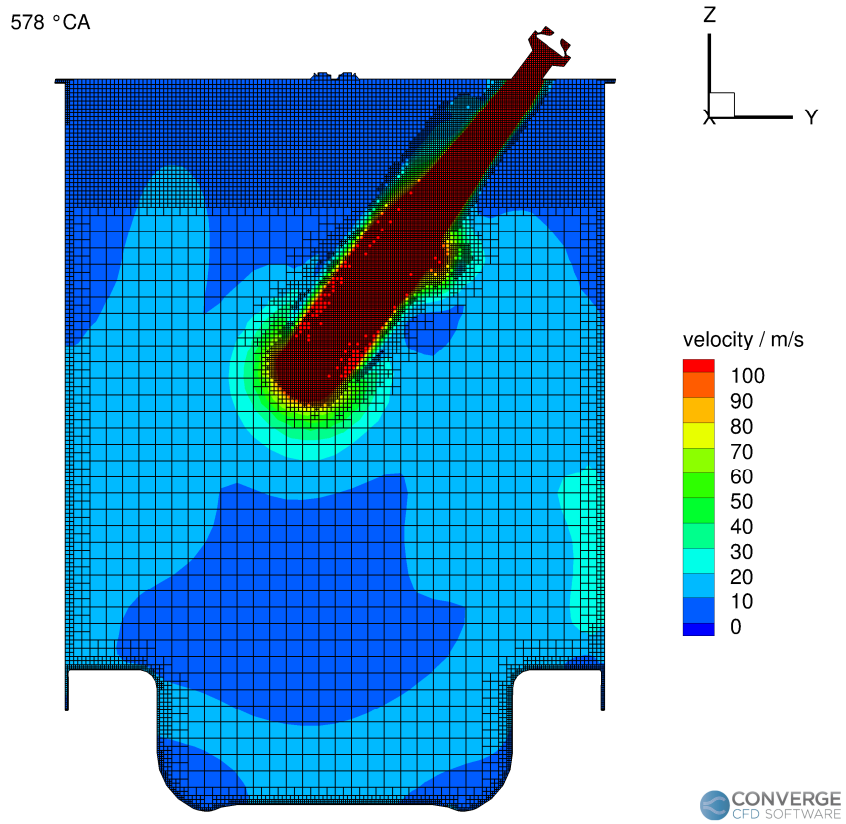


Figure 9. Numerical discretization at 8 °CA after start of injection. Both permanent and adaptive mesh refinements are visible.

Boundary conditions are taken from the test-bench investigations. Measured pressure traces are applied at the inflow and outflow boundaries, at the same locations where the measurements were taken in the experimental engine. The measured in-cylinder pressure trace, together with the other measured quantities such as lambda, is used to validate the setup and boundary conditions of the numerical model. Figure 10 compares the in-cylinder pressures from the test-bench and the numerical simulation. Since the test-bench measurements stem from fired operation, whereas the simulation models only gas exchange, injection and mixing, the data are only comparable up to spark timing ($t_{spark} \cong 10$ °CAbTDC). Up to this point, the two pressure traces deviate by no more than 0.12%. This excellent agreement confirms the geometric accuracy of the model and shows that the boundary conditions for pressure, temperature and injection are applied correctly. The numerical model, therefore, reliably captures the gas exchange process.

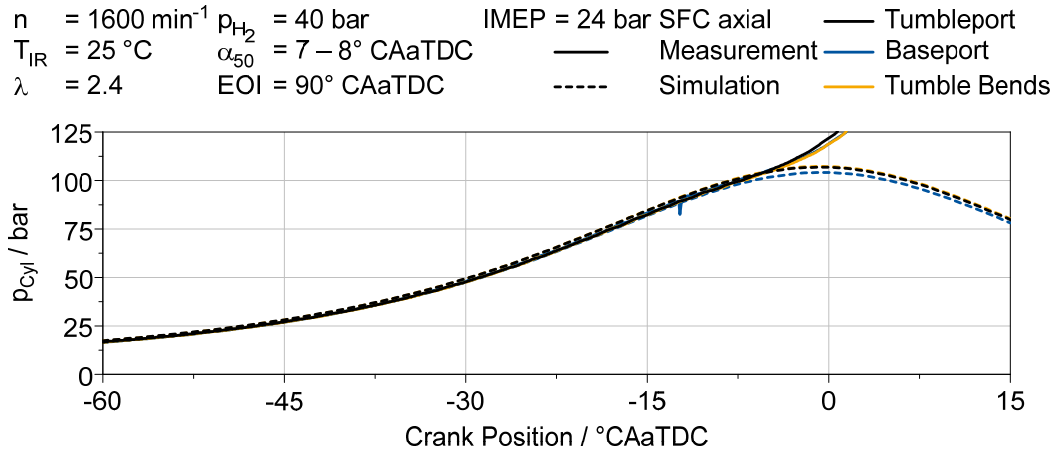


Figure 10. Measured in-cylinder pressure trace and simulated in-cylinder pressure of the gas exchange and mixing simulation.

As the injection is one of the main interests of these investigations, the injector model was not simplified. The injector needle lift is geometrically resolved. A mass flow inlet introduces the hydrogen into the injector, using the hydrogen mass flow from the test bench. They differ slightly from configuration to configuration. The values shown in Table 2 present the average values.

Fixed temperatures are defined for each wall boundary (e.g., cylinder head and liner). These temperatures were kept constant for all three intake port configurations, as no detailed temperature measurements were performed during the experiments. However, previous experimental studies have shown that increasing the charge motion under otherwise constant boundary conditions raises wall temperatures [33]. The in-cylinder temperatures presented later should, therefore, be regarded as conservative estimates. In reality, the tumble port produces even higher temperatures since its wall temperatures would be higher than those of the other two ports.

Data Evaluation

First, a few relevant parameters shall be introduced. The knock amplitude (KA) is evaluated by rectifying the filtered knock signal and calculating the largest amplitude of the cylinder pressure oscillations, as shown in Figure 11. The knock signal is acquired using a high-pass filter with a cutoff frequency of 4571 Hz. The KA_{AV} value is the average knock amplitude of all cycles in a measurement, in this instance, 500 cycles. KA_{High} denotes the maximum amplitude of the 500 measured cycles.

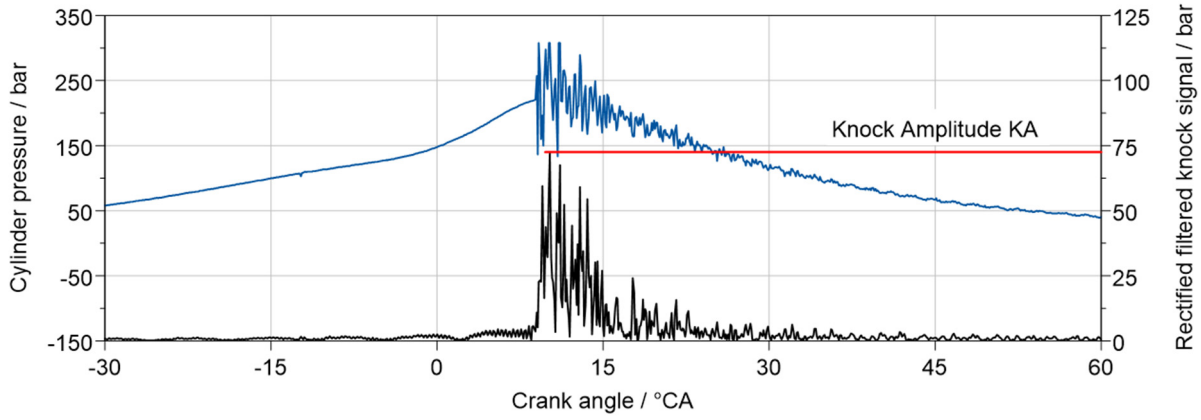


Figure 11. Graphical explanation of the KA value. blue: pressure trace; black: knock signal

The KAMP value is determined by sorting the knock amplitudes of the 500 measured cycles and calculating the desired percentile according to Equation (1). This is illustrated in Figure 12.

$$500 \text{ cycles} \cdot 98.5\% = 492.5 \rightarrow \text{KAMP98.5} = \text{Knock amplitude value of the 493rd cycle} \quad (1)$$

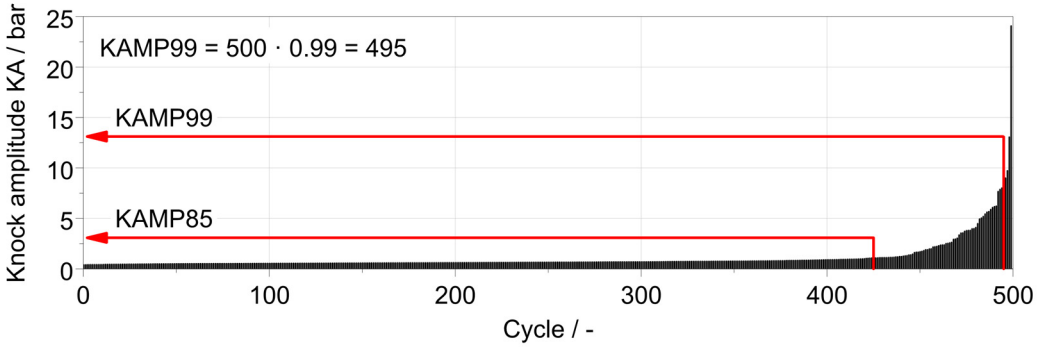


Figure 12. Graphical explanation of the KAMP value.

The pre-ignition frequency is determined based on two criteria. The first criterion uses the 3σ rule for the point of 2% heat release (α_2). If α_2 of a cycle occurs earlier than the average minus three times the standard deviation, it is classified as pre-ignition. The second criterion checks for any heat release prior to the spark timing. If either criterion is met, the cycle is considered a pre-ignition event. These criteria were developed and benchmarked internally and were found to be the most fitting for this specific engine setup.

3. Results and Discussion

3.1. Influence of Charge Motion

In this section, measurements with the axial and angled spray-forming caps performed with the three cylinder heads are discussed. The variations were conducted under the boundary conditions given in the diagram headers. The cylinder heads with their corresponding intake ports were the only hardware components changed during these tests.

3.1.1. Knock

In Figure 13, the knock and pre-ignition (PI) characteristics of a load variation at n = 1600 1/min are displayed. On the right, NO_x emissions, pre-ignition frequency, and the coefficient of variation (COV) of the indicated mean effective pressure (IMEP) are shown. On the left, the maximum and average knock amplitude (KA) values are shown in the first and second graphs. The bottom left diagram illustrates the 98.5th percentile of the knock amplitude (the value of the sorted 493rd cycle). The results clearly indicate that the tumble port is the most sensitive to knock, reaching heavy knock at IMEP = 26 bar, whereas the cylinder heads with less charge motion reach higher loads. Not only does the maximum KA increase earlier, but the average KA and KAMP also show a relative increase within the measurement, indicating that these are not sporadic events but are increasing in frequency. Rising average KA and KAMP values indicate that a knock limit is being reached, where further increases in load could cause engine damage. As the thermal load on the engine structure becomes more critical with higher knock frequencies and peak pressures exerting greater stress on the piston and crank train, the risk of component failure rises. At n = 1600 1/min, it seems that intense charge motion is disadvantageous for combustion, regardless of the SFC used. The TB head shows significant advantages when paired with the axial SFC, increasing the knock limit from IMEP = 30 bar to 32 bar, while simultaneously preventing mega knock events. In contrast, the TP shows better performance with

the angled SFC, but the improvement is less pronounced. The base port does not exhibit significant differences between the two SFCs. The behavior of the TP and the TB suggests that mixture formation strongly influences knock tendency. With poorer mixture formation, more energy is stored in rich zones, which are more prone to auto-ignition and burn significantly faster, leading to higher knock amplitudes. The lower knock limit for the tumble port is also influenced by the higher in-cylinder air temperature due to enhanced heat transfer caused by elevated flow velocities.

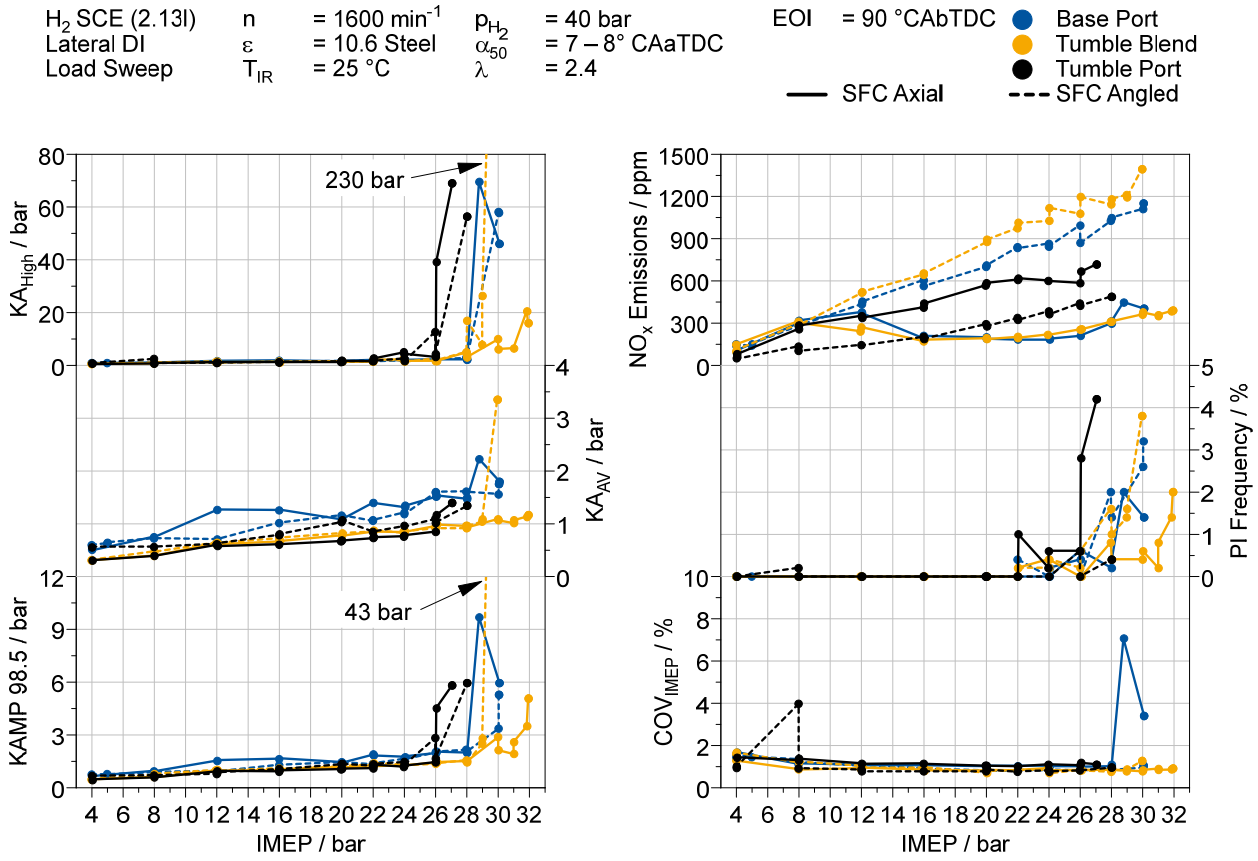


Figure 13. Knock and pre-ignition characteristics of load sweeps with both SFCs and all cylinder heads.

3.1.2. NO_x Emissions

Looking at the top right diagram, the NO_x emissions exhibit remarkable behavior. The base port and tumble blend cylinder heads show high NO_x emissions when paired with the angled SFC and low NO_x emissions with the axial SFC, whereas the trends for the tumble port cylinder head are exactly the opposite. This phenomenon is attributable to poorer mixture formation resulting from the interaction between the injection jet and the charge motion, as well as the interplay with the piston bowl.

In Figure 14, the 3D iso-contours for the different ports are displayed. A $\lambda = 1$ iso-contour highlights the injection spray shape at the end of injection for all combinations of intake ports and spray-forming caps. The top row presents the injection plane, where the lateral injection occurs in the negative zy-direction. The bottom row showcases the tumble plane. Comparing the spray forms between the axial and the angled spray-forming caps for the base port and the tumble blends reveals that the axial spray-forming cap supplies the injection jet with higher inertia. The jet reaches the opposite cylinder wall more rapidly and is pushed upward toward the cylinder head significantly faster. In comparison, the hydrogen jet passing through the angled spray-forming cap is redirected more

downward, possesses less inertia, and remains longer in the lower half of the cylinder. This effect slows down the jet-induced turbulent mixture formation for the angled SFC when used with the base port and the tumble blends, explaining why these configurations produce significantly higher NO_x emissions in the test-bench investigations.

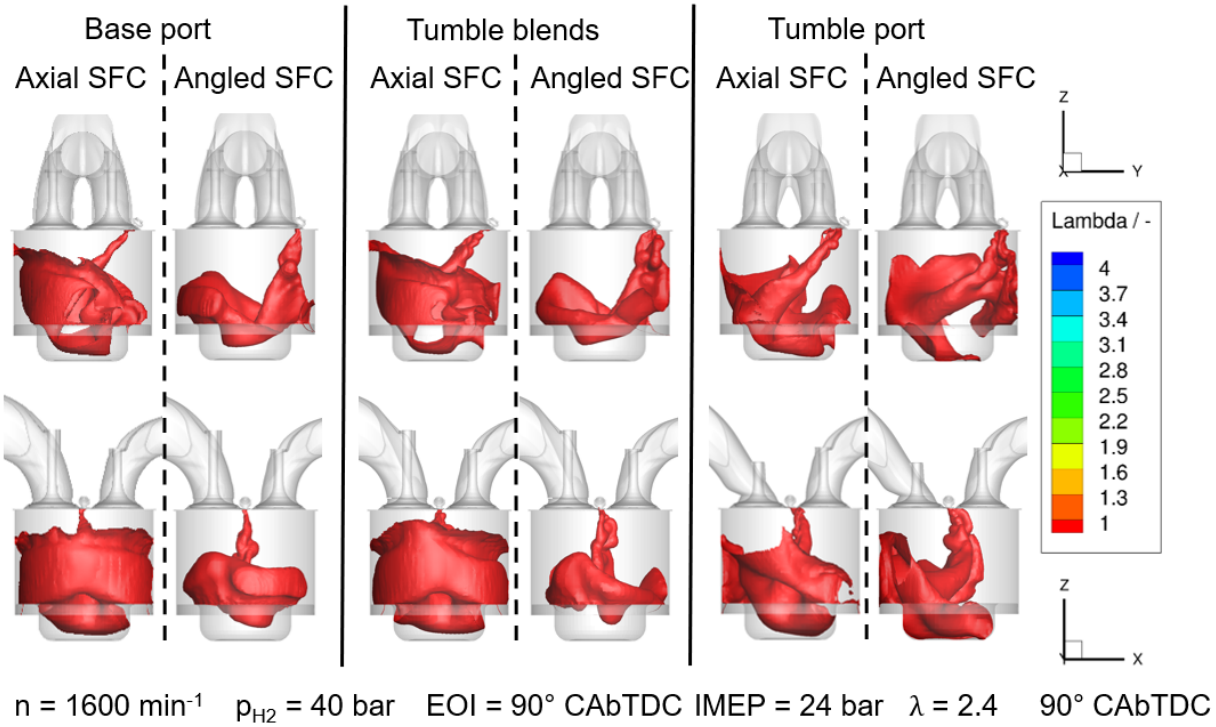


Figure 14. Iso-surface for lambda = 1 for all configurations at end of injection (injection plane (zy) in the top row and tumble plane (zx) in the bottom row).

For the tumble port, no such extreme difference between the two spray-forming caps is observable. As there is still a significant level of charge motion remaining during the injection and compression phases, the mixture formation process is not as dependent on the inertia of the injection jet. Fuel from the piston bowl is brought upward to the cylinder head by the tumble motion; this becomes especially visible in the bottom right images. For the tumble port, this effect is reversed: the NO_x emissions are lower when using the angled spray-forming cap, indicating a more homogeneous mixture formation. The introduction of more charge motion is beneficial in cases with weak jet-induced turbulent mixing (angled SFC). However, for cases where the jet-induced mixture formation process already works well (axial SFC), a further increase in charge motion is not effective.

Figure 15 presents the resulting in-cylinder mixtures for all configurations around the spark timing. The lambda distributions and the COV of Phi match the NO_x emissions perfectly: the combination of low charge motion (base port and tumble blends) and the spray-forming cap with less inertia (angled SFC) results in inadequate mixture formation. At the spark timing, the mixture is still highly inhomogeneous and features some especially rich zones, which explain the increased NO_x emissions for these operating points. Also, the values for the COV of Phi show that there is no significant difference in homogeneity between the base port and the tumble blends. This aligns with the results from Figure 7, where the charge motion introduced by the tumble plates rapidly dissipates and has fallen back down to the levels of the base port at the injection timing.

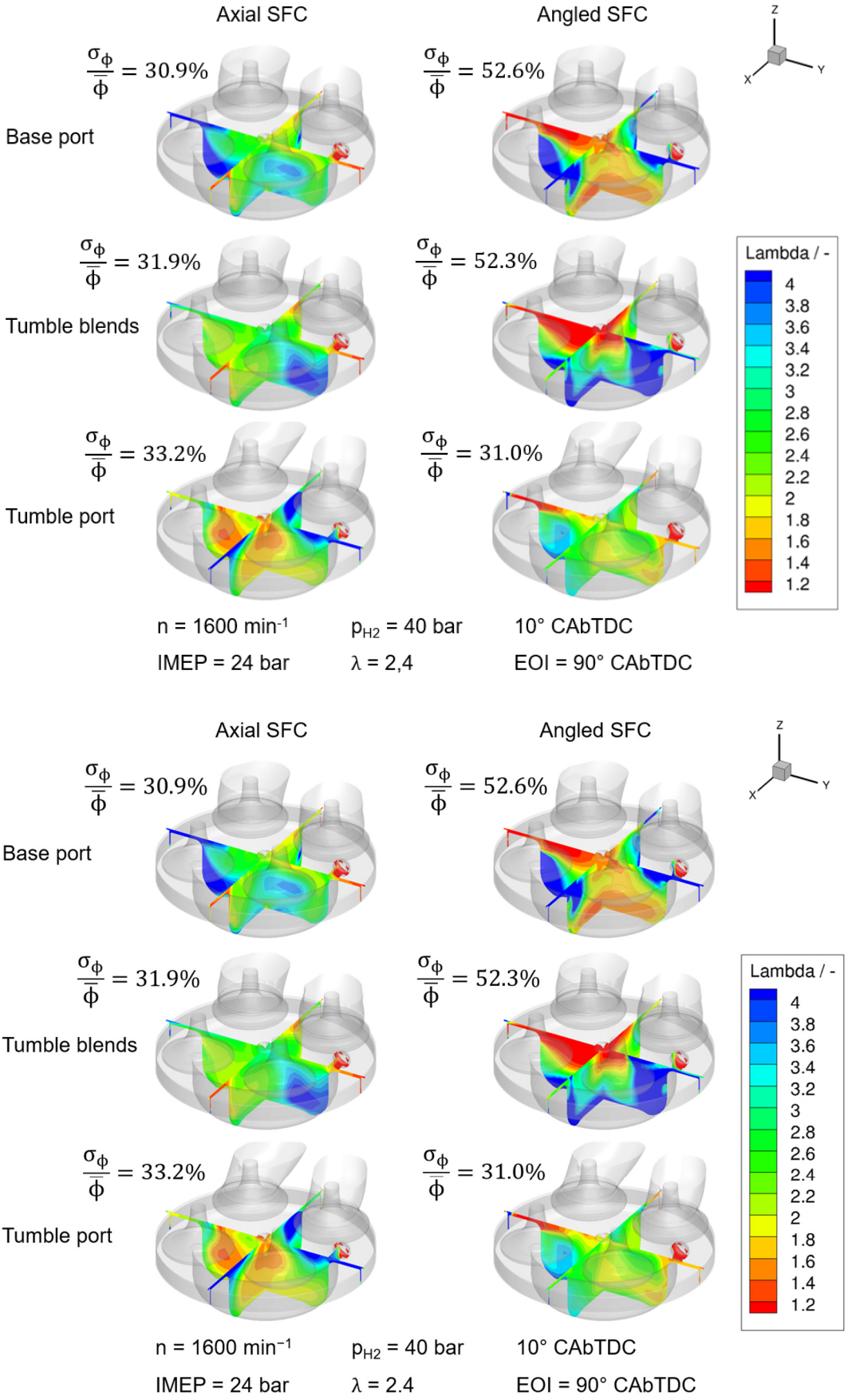


Figure 15. Mixture formation for all configurations at 10 °CAbTDC from CFD simulations.

Overall, these results highlight that for retrofitting a diesel engine for hydrogen operation, it is not necessary to completely redesign the intake port design for maximum charge motion. A well-designed injection cap with enough momentum preservation to support the jet-induced mixture formation can be sufficient. A further increase in charge motion, flow velocities or turbulence does not yield further benefits. It can even be harmful, as the increase in turbulence can accelerate abnormal combustion behavior. The following section presents this in more detail.

3.1.3. Pre-Ignition

The second and third diagrams on the right of Figure 13 show the pre-ignition frequency and the coefficient of variation of IMEP, which represents the combustion stability. As expected, PI frequency rises with load for all hardware configurations. As the wall temperature of the engine rises with load, the heat flux from the wall to the mixture increases during the intake and compression stroke. With higher gas temperatures, more energy is stored in the mixture, reducing the energy that must be supplied by a potential ignition source to induce combustion. The slightly higher PI tendency of the tumble port can also be attributed to the higher gas temperature due to higher wall heat transfer coefficients caused by higher flow velocities.

It is noticeable that most of the pre-ignitions do not increase the COV. These are late PIs that do not reduce the IMEP of the corresponding cycle and, thus, do not have a significant impact on the COV. The high COV values originate from early PI cycles that exhibit a significant fuel burn rate prior to ignition.

In Figure 16, the end of injection (EOI), the current of the ignition coil and the pressure traces of a normal combustion cycle, a late PI, an early PI and a knocking cycle are displayed. For the latter, combustion occurs around 90° CAbTDC (crank angle before top dead center), meaning the engine needs to compress against the combustion, generating reduced or even negative IMEP. This type of PI is critical, as high peak pressures are reached, which can exceed the structural limits of the engine. Early PIs are most likely caused by oil droplets that detach from the piston, evaporate and auto-ignite sporadically. This phenomenon cannot be explained by pure thermal load on the engine, as it can also occur at low load. In Figure 13, the TP with the angled SFC experiences early PI at IMEP = 8 bar. As the engine is being throttled at IMEP = 4 bar, oil can be transported to the combustion chamber, leading to PI when increasing the load [34,35].

Late PI initiates combustion slightly before the ignition timing, which advances the combustion by only a few degrees, and thus, it has only a limited effect on the IMEP. This type of PI is considered less critical for the engine under these conditions if it is not combined with high knock amplitudes. Ignition of late PI cycles is most likely caused by mixture inhomogeneities in combination with high temperatures close to TDC, as these only occur at higher loads.

In the mega knock cycle, combustion does not start significantly earlier than in the average cycle but causes very high knock amplitudes. These usually only occur stochastically, and it is not yet possible to predict mega knock events in this engine.

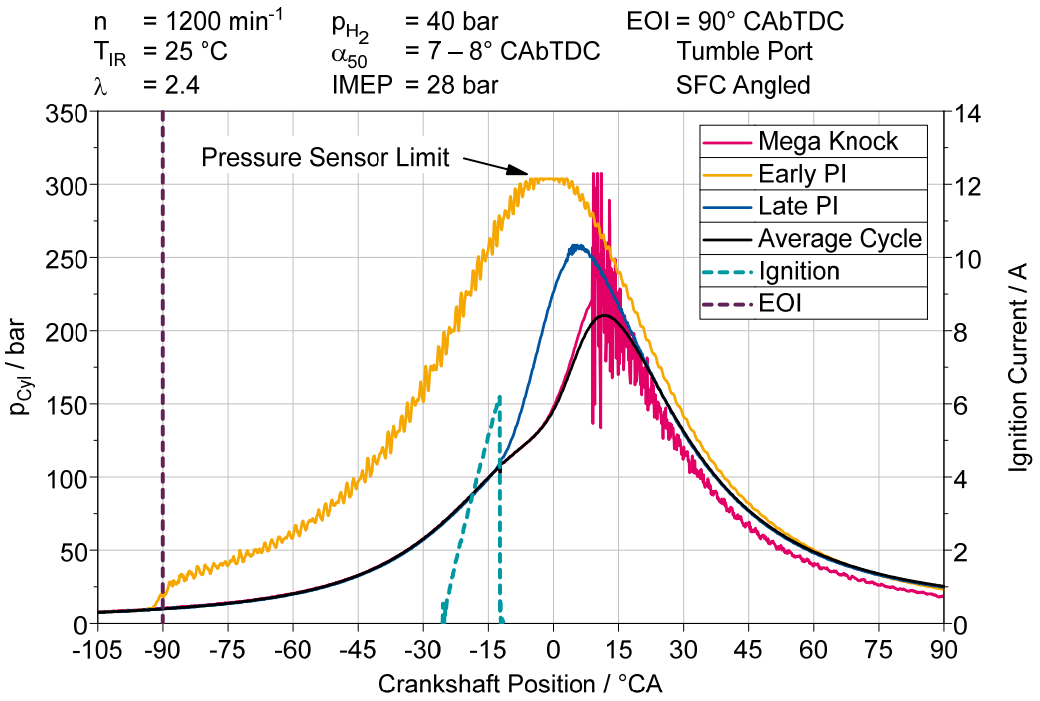


Figure 16. Pressure traces of abnormal combustion phenomena.

In Figure 17, the temperature distribution of the gas at 10° CAbTDC is displayed. As the flow performance decreases from the base to the tumble port according to Figure 6, the flow velocity and intake pressure must be increased to compensate for the lower flow coefficient and to supply the same air mass to the cylinder. The increased flow velocities lead to higher heat transfer coefficients and heat flux from the wall to the gas during the intake and compression stroke, increasing the mixture temperature. As explained in Section 2.2, the temperature comparison is only qualitative, as wall temperatures were kept the same for all three configurations. However, this assumption is conservative, meaning that in reality, the tumble port does produce even hotter gas temperatures.

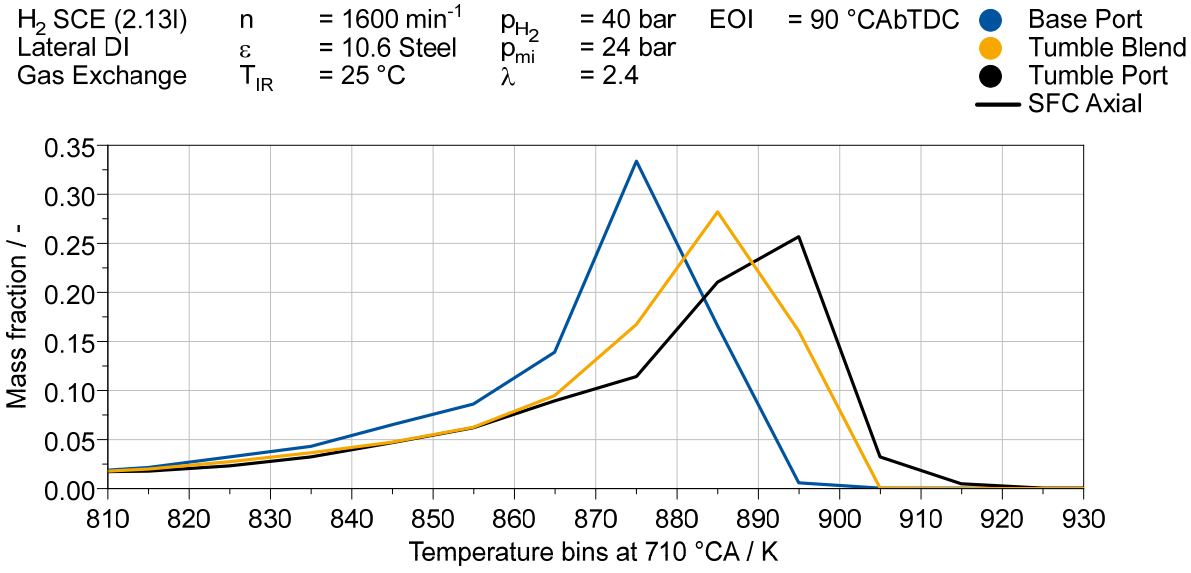


Figure 17. Temperature distribution for all hardware configurations.

3.1.4. Combustion Characteristics

The combustion phasing depicted in Figure 18 is based on the heat release calculated by the indication system. In the diagrams on the left, durations from, e.g., 10% to 50% of the total heat release are displayed. The indices reflect the range shown in the graph. The combustion phasing on the right combines the crank positions of the ignition and various total heat release values in one diagram.

The combustion duration shows unexpected behavior. Due to higher turbulence, the TP should exhibit faster flame propagation. However, this discrepancy is partly caused by flame extinction in the early phase of ignition, leading to a delayed start of combustion.

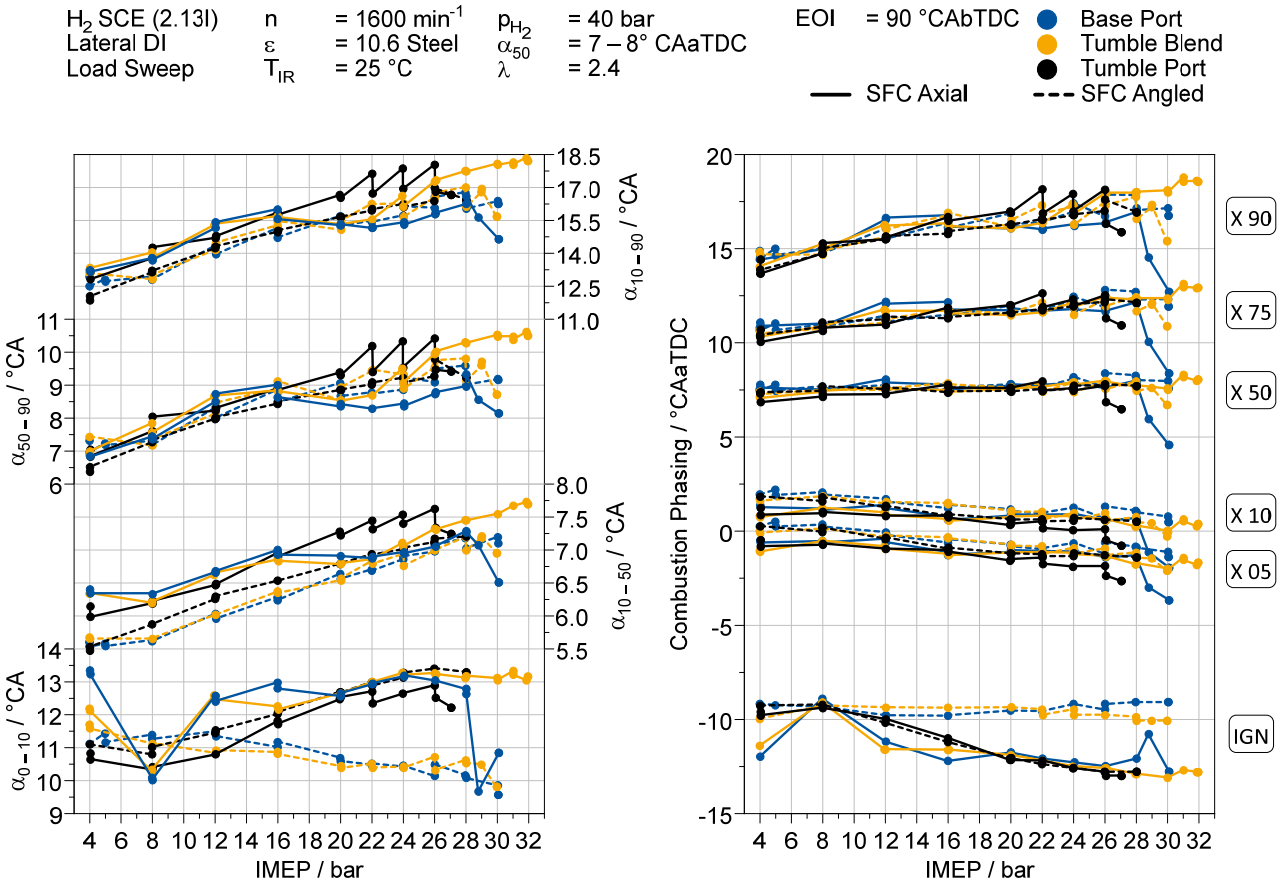


Figure 18. Combustion phasing of load sweeps with both SFCs and all three cylinder heads.

From IMEP = 4–16 bar, the $\alpha_{10\text{-}90}$ window is longer for the axial SFC than for the angled SFC for all cylinder heads. Figure 19 presents the mixture field around spark timing for a load point variation. The left side shows the new load point of IMEP = 16 bar, whereas the right side shows the standard load point of IMEP = 24 bar for comparison. The simulation results for the BP with the axial SFC at IMEP = 16 bar in Figure 19 show that a lean mixture zone is located at the spark plug around the spark timing, leading to poor ignition and early flame kernel development. From 16 bar onwards, the BP and TB with the axial SFC show a trend toward faster combustion while maintaining a constant spark angle. This can be explained by reviewing the mixture formation in Figure 19. The lean zone at the spark plug is eliminated at IMEP = 24 bar, leading to a faster and more stable flame development and an earlier combustion phase.

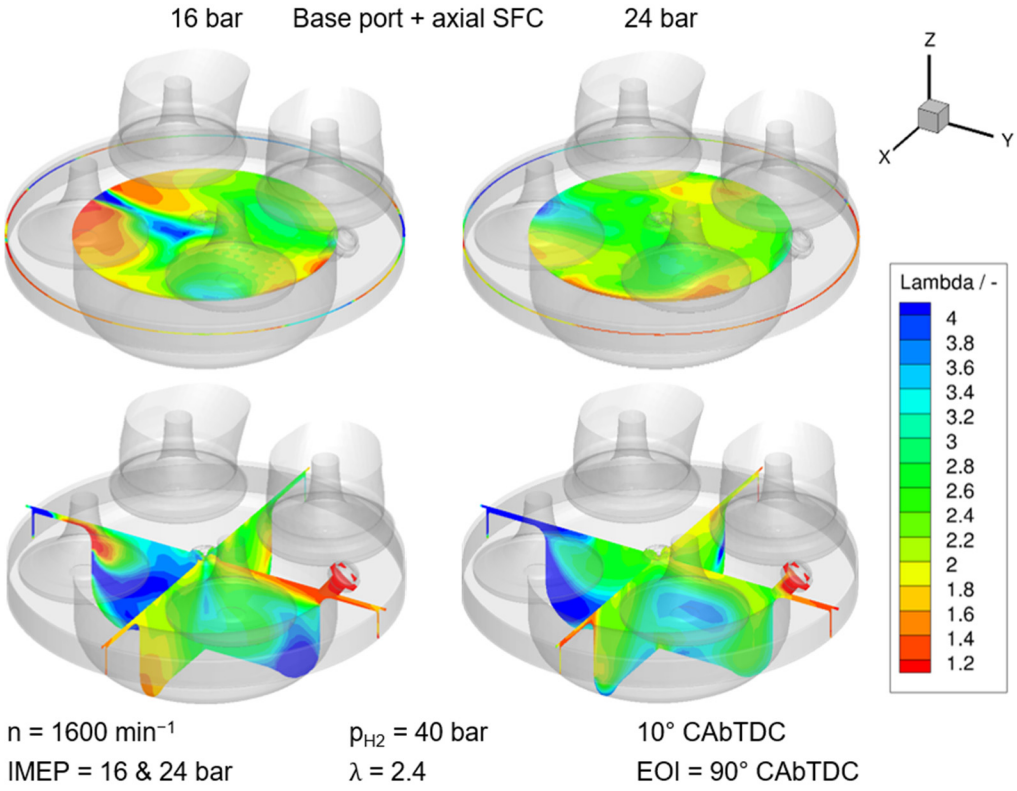


Figure 19. Mixture formation for the base port and the axial SFC for a load point variation (IMEP = 16 and 24 bar).

BP and TB with the angled SFC have rich zones close to the spark plug, leading to fast early combustion; however, due to lean zones at the outer regions of the combustion chamber, the flame cannot develop a spherical shape, leading to slow flame propagation in the late phase of combustion. The tumble port, meanwhile, continues its trend from the lower loads, and the burn duration increases. Reviewing the gas-exchange CFD data of the TP with the axial SFC, a lean mixture cloud is visible that moves towards the spark plug shortly after ignition. This leads to a deceleration of early combustion and partially explains the lack of combustion speed that would otherwise be expected with higher charge motion.

Above IMEP = 16 bar, the $\alpha_{0\text{-}10}$ decreases for the BP and TB with the angled SFC, and the ignition timing was retarded to compensate for the fast early flame kernel development. This indicates a richer mixture at the spark plug, leading to faster flame development, which is supported by the graphs in Figure 15. The early and late phases of combustion show a consistent trend, with the burn duration increasing for these two configurations.

Ultimately, it becomes clear that slower combustion is, in this case, the result of inadequate mixture formation, where lean and rich zones interact with the flame. Consequently, faster combustion can result from a favorable mixture formation if lean zones that hinder flame development are successfully eliminated.

3.2. Influence of Gas Temperature

As previously mentioned, the gas temperature has a strong influence on abnormal combustion, as the energy in the mixture is increased and the gap between the auto-ignition temperature and gas temperature decreases. In Figure 20, two load sweeps with the tumble port and the angled SFC at different intake temperatures, T_{IR} = 25 °C and 40 °C, are displayed. It becomes clear that with elevated intake temperatures, the knock and pre-

ignition tendency increase significantly. This supports the theory that the higher intake gas temperature of the tumble port leads to a higher tendency for abnormal combustion. Higher maximum knock amplitudes occur at a 40 °C intake temperature, as well as a much higher knock frequency, as indicated by the high KAMP and average KA values.

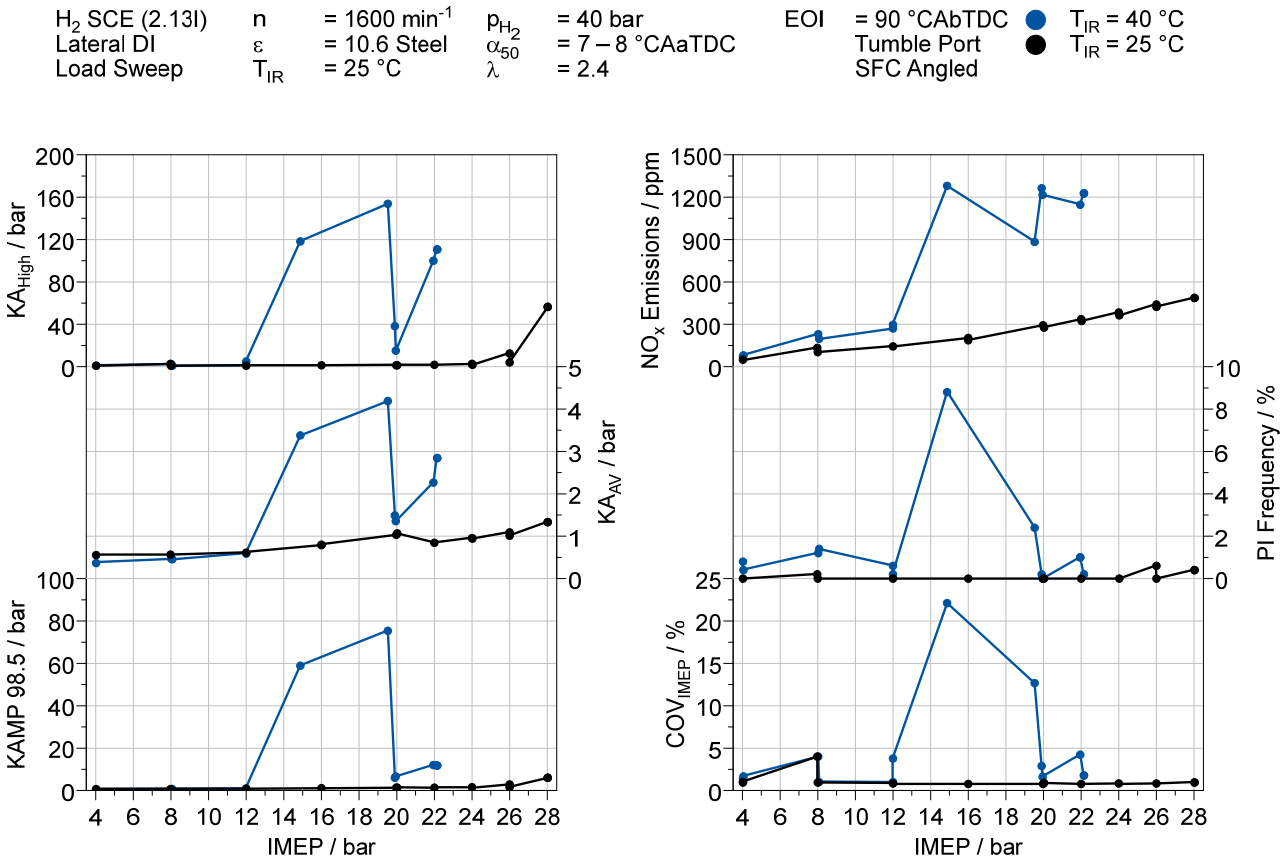


Figure 20. Knock and pre-ignition characteristics of load sweeps with different intake temperatures.

During this measurement, another interesting investigation was carried out. In the pursuit of achieving higher loads and suppressing early pre-ignition, the end of injection at IMEP = 20 bar was retarded even further from 90° to 70 °CAbTDC. The injection parameters are displayed in Figure 21. The investigations showed that there is no combustion during injection, but only shortly after it, suggesting that the late injection could suppress pre-ignition. This theory proved true, and the rate of early PI reduced significantly, as is visible in the lower COV and PI frequency in Figure 20. There are three main factors for this. Firstly, there is less time for the hydrogen–air mixture to heat up, as hydrogen is added to the combustion chamber at a later crank position. Secondly, higher velocities and turbulence during injection might suppress flame kernel development. Thirdly, the mixture could reach a potential ignition source later or not at all. The downside to this strategy is that the mixture formation becomes very poor, and NO_x emissions without abnormal combustion are on the same level as before with abnormal combustion.

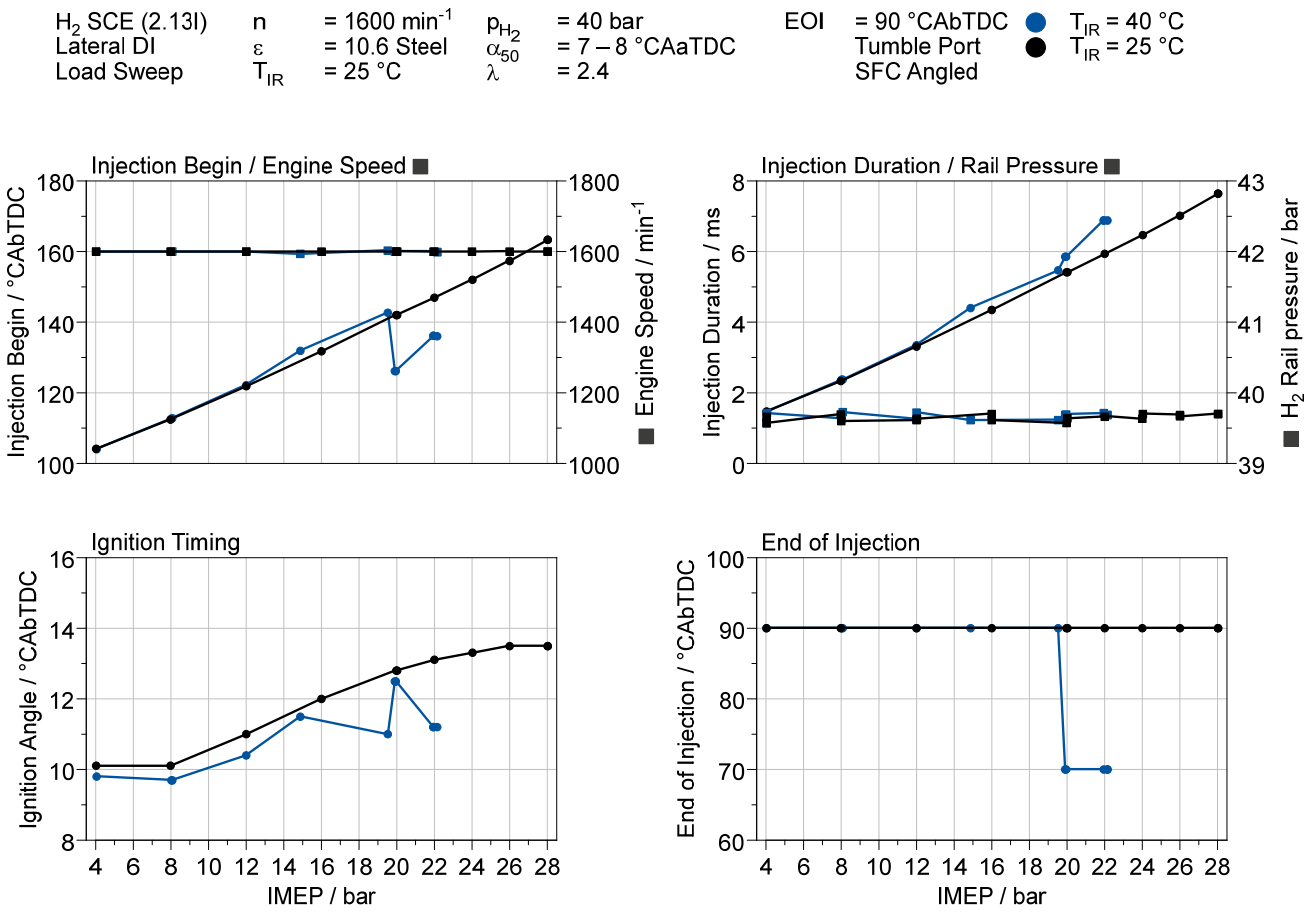


Figure 21. Injection parameters of load variation at different intake temperatures.

Another interesting topic to mention is the influence of abnormal combustion on emissions. In Figure 22, the relevant emissions from the measurement are displayed. Aside from NO_x emissions, unburned hydrocarbons (HCs) and carbon monoxide (CO) emissions are also elevated. As the only source of carbon-based emissions in a hydrogen engine is engine oil, the trends suggest increased oil consumption due to abnormal combustion. One of the reasons is a higher rate of oil evaporation from the cylinder walls. Another reason might be oil sitting in the top land on the piston crown that is shaken off by the pressure oscillations induced by knocking combustion. Hydrogen emissions increase due to retarded injection timing, which results in poorer mixture formation and more flame quenching.

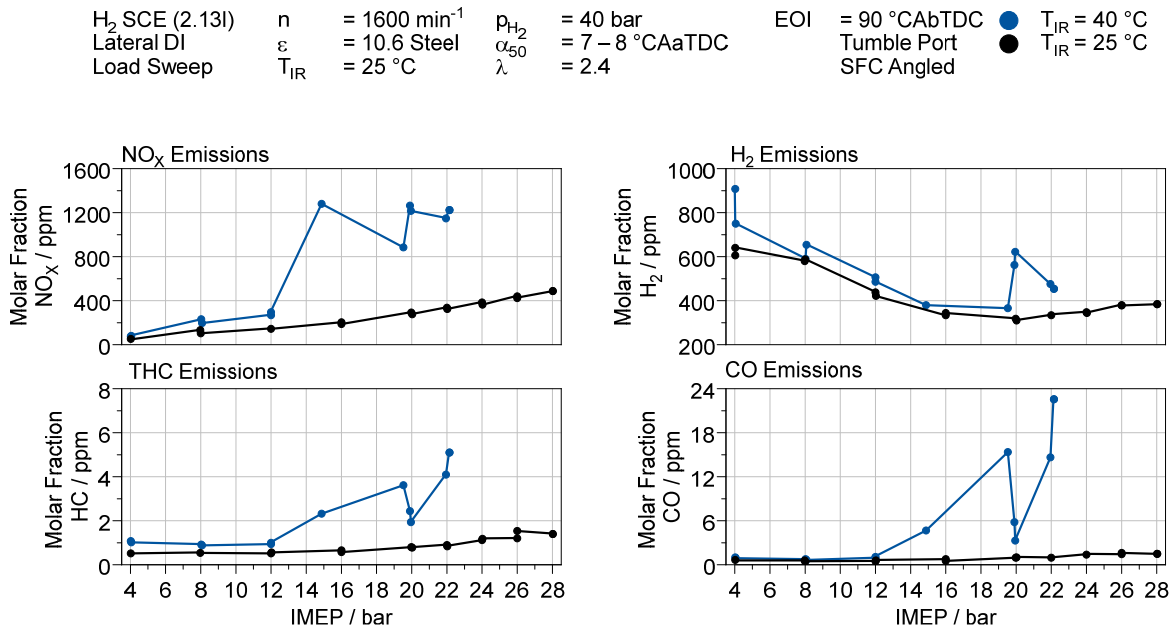


Figure 22. Influence of heavy abnormal combustion on emission behavior.

4. Discussion

In previous investigations on this engine, charge motion was found to reduce the tendency towards abnormal combustion at a medium load and turbulence level. In those investigations, previous generations of injectors were used that featured lower flow rates than the current injector. It was also shown previously that injectors with higher flow rates are beneficial for mixture formation and robustness against abnormal combustion [36].

It is also notable that those earlier investigations were performed with a constant start of injection of 170 °CAbTDC, which is significantly earlier than during the current investigations, thereby providing more time for homogenization. The shift to late injections was necessitated by the occurrence of highly frequent early pre-ignitions, which made engine operation impossible.

It was also previously found that a higher intake temperature increases the tendency for abnormal combustion. During ignition variations, heavy knock was recorded at α_{50} = 6 °CAaTDC with T_{IR} = 40 °C, while no severe knock was recorded at α_{50} = 0 °CAaTDC with T_{IR} = 25 °C. Meanwhile, pre-ignitions showed a steeper incline with higher temperatures at late ignition timings [37]. Similar results are reported by other researchers in the literature [1,38].

In this regard, the results presented in this paper are consistent with previous findings, providing deeper insights into the role of charge motion in combustion system development for hydrogen internal combustion engines of the heavy-duty class.

However, one main difference in comparison with previous investigations is that an increase in charge motion does not always reduce the tendency for abnormal combustion at all operating points. When the spray cap design already produces a good level of homogenization, further enhancing the mixing via charge motion and turbulence is unnecessary. In fact, combustion behavior then worsens, as the injection jet and the charge motion can influence each other in a negative fashion. This is visible in the experimental data, where the axial SFC performs well with the base port and the blends port, whereas the axial SFC combined with the tumble port is limited earlier due to knocking. The angled SFC combined with the low charge-motion ports exhibits poor performance, and NO_x emissions are high. In this case, increasing the charge motion to a higher level does improve the combustion process.

The CFD investigations explain these observations in more detail by visualizing the injection jet, the interaction with the charge motion, and the turbulent mixing. The combustion systems that produce high NO_x emissions in the test bench investigations all exhibit significant inhomogeneity and local rich zones. It is also visible how the increase in charge motion from the tumble port interacts with the axial spray guiding cap in an unfavorable manner. The fuel remains in the piston bowl longer, and mixing is worsened.

Overall, the results highlight that the injector, the spray-guiding cap, and the charge motion concept need to be considered holistically during design of a hydrogen combustion engine. While charge motion can improve mixing, and thereby improve combustion behavior and decrease emissions, it is not true that a further increase in charge motion is always beneficial. If the injection has sufficient impulse and a well-designed spray-guiding cap to achieve good mixing, a further increase in charge motion can counteract this system. On the test bench, this effect was shown by knocking and increased NO_x emissions. The CFD simulations visualized this effect and aligned well with the test bench results, showcasing that the employed CFD methodology is a reliable tool to evaluate different hydrogen combustion systems.

5. Conclusions

It can be concluded that increasing tumble ratios to high levels by adapting the intake port design in a heavy-duty engine with a flat flame deck can lead to higher mixture temperatures due to increased wall heat transfer during the intake and compression stroke. These increased temperatures amplify the occurrence of abnormal combustion. Meanwhile, charge motion increases the robustness against less-than-ideal injector spray targeting by improving mixture formation due to turbulence, whereas low-charge-motion concepts rely more on the interaction between the hydrogen jet and the combustion chamber. This results in increased NO_x emissions if the spray targeting is not optimized.

Overall, in this study, the achievable load decreased for the highest charge motion setup by 6 bar down to IMEP = 26 bar.

These findings suggest that retrofitting commercial diesel engines to operate with hydrogen is possible without a major redesign of the cylinder head and intake ports if the injection system is designed carefully.

Future work should focus on improving the robustness against early pre-ignition, so that early injection timings can be realized to utilize the benefits of tumble during the early intake stroke. Furthermore, the effects of impaired ignition and early flame kernel development should be investigated to enhance the positive effects of increased turbulence on combustion. Also, the CFD investigations in this work were purely RANS mixture formation simulations. Future studies will employ multi-cycle LES and combustion simulations to resolve cycle-to-cycle fluctuations.

Author Contributions: Conceptualization, P.Z. and M.L.; methodology, P.Z. and M.L.; investigation, P.Z. and M.L.; writing—original draft preparation, P.Z. and M.L.; writing—review and editing, P.Z., M.L., and S.P.; project administration and funding acquisition, S.P. All authors have read and agreed to the published version of the manuscript.

Funding: This research was funded by CORNET/BMWE/IGF—Federal Ministry for Economic Affairs and Energy/Industrial Collective Research/International (grant number: 01IF00403C), and FVV-EM—FVV projects—funded from own resources (grant number: 6015413). Open-access funding was provided by the Open-Access Publishing Fund of RWTH Aachen University.

Data Availability Statement: The original data presented in this study are openly available in RWTH Publications at https://doi.org/10.18154/RWTH-2026-08826.

Acknowledgments: The authors would like to thank the test bench technicians Alexander Lemm and Robert Schell for supporting testing activities, the student workers Sebastian Faber and Thorben Strzoda for supporting data organization, ACTech GmbH for supporting the development and manufacturing of the tumble port cylinder head, FEV Group GmbH for supporting testing and development activities, Robert Bosch GmbH for supplying the injector, and Hydac International GmbH for supplying parts of the hydrogen system. The authors would also like to thank the German Federal Ministry of Research, Technology and Space and the German federal states (https://go-nhr.de/our-partners (accessed on 2nd November 2026)) for supporting this work/project as part of the National High-Performance Computing (NHR) joint funding program. Convergent Science provided CONVERGE licenses and technical support for this work.

Conflicts of Interest: The authors declare no conflicts of interest. The funders had no role in the design of this study; in the collection, analysis, or interpretation of the data; in the writing of this manuscript; or in the decision to publish the results.

Abbreviations

The following abbreviations are used in this manuscript:

H2	Hydrogen
DI	Direct injection
ICE	Internal combustion engine
IMEP	Indicated mean effective pressure
TDC	Top dead center
°CA	Degree crank angle
°CAbTDC	Degree crank angle before top dead center
°CAaTDC	Degree crank angle after top dead center
NOx	Sum of nitrous oxide and nitrous dioxide
3D	3-dimensional
CFD	Computational fluid dynamics
SI	Spark ignition
HD	Heavy duty
PI	Pre-ignition
EGR	Exhaust gas recirculation
MIE	Minimum ignition energy
SCE	Single-cylinder engine
CR	Compression ratio
SFC	Spray-forming cap
BP	Base port
TB	Tumble blend
TP	Tumble port
RANS	Reynolds-averaged Navier–Stokes
RNG	Re-normalization group
CFL	Courant–Friedrichs–Lewy
PSIO	Pressure-implicit with splitting of operators
KA	Knock peak to peak
COV	Coefficient of variation
KAMP	Knock amplitude sorted
EOI	End of injection
HC	Hydrocarbon
CO	Carbon monoxide
T_{IR}	Intake runner temperature

References

1. Park, H.; Lee, J.; Oh, S.; Kim, C.; Park, Y.; Yoo, D. Strategies of hydrogen-air mixture formation for suppressing backfire, pre-ignition, and knock in full-load operations of hydrogen heavy-duty engines. *Energy* **2025**, *326*, 136343. https://doi.org/10.1016/j.energy.2025.136343.
2. Goyal, H.; Jones, P.; Bajwa, A.; Parsons, D.; Akehurst, S.; Davy, M.H.; Leach, F.C.; Esposito, S. Design trends and challenges in hydrogen direct injection (H2DI) internal combustion engines—A review. *Int. J. Hydrogen Energy* **2024**, *86*, 1179–1194. https://doi.org/10.1016/j.ijhydene.2024.08.284.
3. Guo, S.; Liu, J.; Zhao, C.; Wang, L.; Yang, Z. Research on pre-ignition in hydrogen internal combustion engines based on characteristic parameters of hot spot. *Int. J. Hydrogen Energy* **2024**, *65*, 548–554. https://doi.org/10.1016/j.ijhydene.2024.03.375.
4. Zhang, S.; Sun, B.; Luo, Q.; Bao, L. Experimental evaluation of pre-ignition and multi-objective optimal controlling of turbocharged direct injection hydrogen engines under high-load and high-speed conditions using Taguchi and TOPSIS methods. *Energy Convers. Manag.* **2025**, *325*, 119378. https://doi.org/10.1016/j.enconman.2024.119378.
5. Duan, Y.; Luo, Q.; Zhang, S.; Sun, B.; Bao, L.; Li, S.; Zhang, J.; Bu, Y. Study on multi-cylinder pre-ignition characteristics and pre-ignition induced super knock mechanism of direct injected hydrogen engines. *Appl. Therm. Eng.* **2026**, *290*, 130092. https://doi.org/10.1016/j.applthermaleng.2026.130092.
6. Zhao, W.; Ao, C.; Ruan, S.; Zhang, L.; Ji, Q.; Liu, J. Taming the "hydrogen flame": A review on the mechanism and cutting-edge suppression strategies of abnormal combustion in H2 engines. *Renew. Sustain. Energy Rev.* **2026**, *238*, 117095. https://doi.org/10.1016/j.rser.2026.117095.
7. Bane, S.; Shepherd, J.E.; Kwon, E.; Day, A.C. Statistical analysis of electrostatic spark ignition of lean H2/O2/Ar mixtures. *Int. J. Hydrogen Energy* **2011**, *36*, 2344–2350. https://doi.org/10.1016/j.ijhydene.2010.05.082.
8. Maas, U.; Warnatz, J. Ignition processes in hydrogen oxygen mixtures. *Combust. Flame* **1988**, *74*, 53–69. https://doi.org/10.1016/0010-2180(88)90086-7.
9. Chu, H.; Li, T.; Bai, H.; Li, Z.; Pitsch, H. Numerical investigation of hot-spot surface ignition of hydrogen-air mixtures. *Proc. Combust. Inst.* **2025**, *41*, 105903. https://doi.org/10.1016/j.proci.2025.105903.
10. Golc, D.; Esposito, S.; Khosravi, M.; Beeckmann, J.; Pitsch, H. Investigation of hot-spot-induced pre-ignition in methanol- and hydrogen-fueled spark-ignition engines. *Proc. Combust. Inst.* **2025**, *41*, 105932. https://doi.org/10.1016/j.proci.2025.105932.
11. Wang, S.; Li, Y.; Li, M.; Wang, H. Realizing the diffusion combustion through the pre-chamber: Towards heavy-duty hydrogen engines. *Appl. Therm. Eng.* **2025**, *280*, 128225. https://doi.org/10.1016/j.applthermaleng.2025.128225.
12. Menaca, R.; Liu, X.; Mohan, B.; Zhang, A.; Silva, M.; Shakeel, M.R.; AlRamadan, A.S.; Cenker, E.; Pei, Y.; Im, H.G. Data-driven co-optimization of piston and pre-chamber in a heavy-duty hydrogen engine. *Int. J. Hydrogen Energy* **2025**, *189*, 152082. https://doi.org/10.1016/j.ijhydene.2025.152082.
13. Liang, Y.; Xing, K.; Huang, H.; Ning, D.; Wang, Y.; Wang, X. Investigation of knock combustion mechanism and injection angle optimization in a heavy-duty direct-injection hydrogen engine. *Energy* **2025**, *335*, 138041. https://doi.org/10.1016/j.energy.2025.138041.
14. Piano, A.; Pucillo, F.; Millo, F.; Giordana, S.; Rapetto, N.; Schuette, C. Experimental investigation on the optimal injection and combustion phasing for a direct injection hydrogen-fuelled internal combustion engine for heavy-duty applications. *Int. J. Hydrogen Energy* **2025**, *100*, 398–406. https://doi.org/10.1016/j.ijhydene.2024.12.194.
15. Zhu, G.; Gao, Y.; Chen, W.; Zuo, Q.; Shi, R.; Kou, C.; Wang, H.; Shen, Z.; Ning, D. Effects of VVT-based internal EGR on combustion and knock characteristics of a heavy-duty hydrogen direct injection engine. *Fuel* **2027**, *429*, 140832. https://doi.org/10.1016/j.fuel.2026.140832.
16. Serrano, D.; Giuffrida, V.; Laget, O.; Gautrot, X. Comprehensive experimental and numerical investigation on a dedicated hydrogen combustion system for heavy duty application. *Int. J. Engine Res.* **2026**, *27*, 1270–1289. https://doi.org/10.1177/14680874251353554.
17. Zhao, L.; Zhang, A.; Sari, R.L.; Popuri, S.S.; Bowen, N.; Matuszak, G. Simulated-based combustion system development in a direct-injection spark-ignited hydrogen engine. *Fuel* **2025**, *388*, 134434. https://doi.org/10.1016/j.fuel.2025.134434.
18. Menaca, R.; Silva, M.; Panithasan, M.; Liu, X.; Zaihi, A.; Cenker, E.; Qahtani, Y.A.; Syed, I.; Pei, Y.; Turner, J.W.; et al. Mixing and combustion dynamics in a heavy-duty hydrogen direct-injection engine. *Appl. Therm. Eng.* **2026**, *300*, 131535. https://doi.org/10.1016/j.applthermaleng.2026.131535.

19. Bunce, M.; Seba, B.; Andreutti, R.; Yan, Z.; Peters, N. Development of a High Power, Low Emissions Heavy Duty Hydrogen Engine. In Proceedings of the WCX SAE World Congress Experience, Detroit, MI, USA, 16–18 April 2024. https://doi.org/10.4271/2024-01-2610.
20. Ono, R.; Nifuku, M.; Fujiwara, S.; Horiguchi, S.; Oda, T. Minimum ignition energy of hydrogen–air mixture: Effects of humidity and spark duration. *J. Electrost.* **2007**, *65*, 87–93. https://doi.org/10.1016/j.elstat.2006.07.004.
21. Moorhouse, J.; Williams, A.; Maddison, T.E. An investigation of the minimum ignition energies of some C1 to C7 hydrocarbons. *Combust. Flame* **1974**, *23*, 203–213. https://doi.org/10.1016/0010-2180(74)90058-3.
22. Thewes, M.; Virnich, L.; Dhongde, A.J.; Boberic, A.; Zimmer, P.M.M.; Pischinger, S. Is 30 Bar Mean Effective Pressure the Limit for Spark Ignited Commercial Hydrogen Engines?/Ist bei 30 bar Mitteldruck das Limit für fremdgezündete Nutzfahrzeugwasserstoffmotoren erreicht? In Proceedings of the 46th International Vienna Motor Symposium, Vienna, Austria, 14–16 May 2025. https://doi.org/10.62626/3ce4-qcpb.
23. Richards, K. J., Senscal, P. K., and Pomraning, E., CONVERGE 3.0 Manual, Convergent Science, Madison, WI (2020).
24. Addepalli, S.K.; Pei, Y.; Zhang, Y.; Scarcelli, R. Multi-dimensional modeling of mixture preparation in a direct injection engine fueled with gaseous hydrogen. *Int. J. Hydrogen Energy* **2022**, *47*, 29085–29101. https://doi.org/10.1016/j.ijhydene.2022.06.182.
25. Le Moine, J.; Senecal, P.K.; Kaiser, S.A.; Salazar, V.M.; Anders, J.W.; Svensson, K.I.; Gehrke, C.R. A Computational Study of the Mixture Preparation in a Direct–Injection Hydrogen Engine. *J. Eng. Gas Turbines Power* **2015**, *137*, 111508. https://doi.org/10.1115/1.4030397.
26. Babayev, R.; Andersson, A.; Dalmau, A.S.; Im, H.G.; Johansson, B. Computational characterization of hydrogen direct injection and nonpremixed combustion in a compression-ignition engine. *Int. J. Hydrogen Energy* **2021**, *46*, 18678–18696. https://doi.org/10.1016/j.ijhydene.2021.02.223.
27. Houidi, M.B.; Moreno-Cabezas, K.; Zaihi, A.; Aljohani, B.; Wu, H.; AlRamadan, A.; Cenker, E.; Im, H.G.; Roberts, W.L. Investigating hydrogen direct injection technology: A comparative analysis of nozzle geometries for enhanced mixing in internal combustion engines. *Proc. Combust. Inst.* **2024**, *40*, 105631. https://doi.org/10.1016/j.proci.2024.105631.
28. Bonelli, F.; Viggiano, A.; Magi, V. A Numerical Analysis of Hydrogen Underexpanded Jets Under Real Gas Assumption. *J. Fluids Eng.* **2013**, *135*, 121101. https://doi.org/10.1115/1.4025253.
29. Hamzehloo, A.; Aleiferis, P. Computational Study of Hydrogen Direct Injection for Internal Combustion Engines. In Proceedings of the SAE/KSAE 2013 International Powertrains, Fuels & Lubricants Meeting, Seoul, Republic of Korea, 21–23 October 2013. https://doi.org/10.4271/2013-01-2524.
30. Laichter, J.; Kaiser, S.A. Optical Investigation of the Influence of In-cylinder Flow and Mixture Inhomogeneity on Cyclic Variability in a Direct-Injection Spark Ignition Engine. *Flow Turbul. Combust* **2023**, *110*, 171–183. https://doi.org/10.1007/s10494-022-00344-8.
31. Reinbold, M.; Liang, M.; Bucherer, M.; Wijeyakulasuriya, S.; Bui, T.; Senecal, K.; Koch, T. Numerical simulation and experimental validation of NO emissions in a heavy-duty H2DI engine considering injector needle dynamics and multi-cycle analysis. *Automot. Engine Technol.* **2026**, *11*, 3. https://doi.org/10.1007/s41104-025-00165-7.
32. Esposito, S.; Mally, M.; Cai, L.; Pitsch, H.; Pischinger, S. Validation of a RANS 3D-CFD Gaseous Emission Model with Space-, Species-, and Cycle-Resolved Measurements from an SI DI Engine. *Energies* **2020**, *13*, 4287. https://doi.org/10.3390/en13174287.
33. Broatch, A.; Olmeda, P.; García, A.; Salvador-Iborra, J.; Warey, A. Impact of swirl on in-cylinder heat transfer in a light-duty diesel engine. *Energy* **2017**, *119*, 1010–1023. https://doi.org/10.1016/j.energy.2016.11.040.
34. Meske, P.R.; Schmidt, K.; Shiba, H.; Capellmann, D.R.; Retzlaff, M.; Zimmer, P.; Boberic, A.; Pischinger, P.S.; Virnich, D.L. Component and Combustion Optimization of a Hydrogen Internal Combustion Engine to Reach High Specific Power for Heavy-Duty Applications. In Proceedings of the 2023 JSAE/SAE Powertrains, Energy and Lubricants International Meeting, Kyoto, Japan, 29 August–1 September 2023. https://doi.org/10.4271/2023-32-0038.
35. Thirouard, B.; Tian, T. Oil Transport in the Piston Ring Pack (Part I): Identification and Characterization of the Main Oil Transport Routes and Mechanisms. In Proceedings of the 2003 JSAE/SAE International Spring Fuels and Lubricants Meeting, Yokohama, Japan, 19–22 May 2003. https://doi.org/10.4271/2003-01-1952.
36. Koerfer, T.; Dhongde, A.; Boberic, A.; Zimmer, P.; Pischinger, S. Sustainable Engines with Carbon-Neutral Fuels—Fast Adaptation for Efficient Multi-Fuel Operation by Tailored Charge Motion Design. In *SAE Technical Paper Sustainable Energy & Powertrains*; SAE International: Troy, MI, USA, 2025. https://doi.org/10.4271/2025-01-0534.

37. Koerfer, T.; Zimmer, P.; Li, Z.; Pischinger, S.; Lückerath, M. Lifting the Key Functional Figures Concerning Performance and Efficiency for 2nd Gen. H_2 Engines for On- and Off-Highway Installations by Tailored Engineering Measures. In Proceedings of the 17th International Conference on Engines and Vehicles, Capri, Italy, 14–17 September 2025. https://doi.org/10.4271/2025-24-0049.
38. Liu, J. Introduction of Abnormal Combustion in Hydrogen Internal Combustion Engines and the Detection Method. *Trends Renew. Energy* **2022**, *8*, 38–48. https://doi.org/10.17737/tre.2022.8.1.00136.

Disclaimer/Publisher's Note: The statements, opinions and data contained in all publications are solely those of the individual author(s) and contributor(s) and not of MDPI and/or the editor(s). MDPI and/or the editor(s) disclaim responsibility for any injury to people or property resulting from any ideas, methods, instructions or products referred to in the content.